

# Data-Driven CFD Modeling of Turbulent Flows Through Complex Structures

Jian-Xun Wang, Heng Xiao\*

*Department of Aerospace and Ocean Engineering, Virginia Tech, Blacksburg, VA 24060, United States*

---

## Abstract

The growth of computational resources in the past decades has expanded the application of Computational Fluid Dynamics (CFD) from the traditional fields of aerodynamics and hydrodynamics to a number of new areas. Examples range from the heat and fluid flows in nuclear reactor vessels and in data centers to the turbulence flows through wind turbine farms and coastal vegetation plants. However, in these new applications complex structures are often exist (e.g., rod bundles in reactor vessels and turbines in wind farms), which makes fully resolved, first-principle based CFD modeling prohibitively expensive. This obstacle seriously impairs the predictive capability of CFD models in these applications. On the other hand, a limited amount of measurement data is often available in the systems in the above-mentioned applications. In this work we propose a data-driven, physics-based approach to perform full field inversion on the effects of the complex structures on the flow. This is achieved by assimilating observation data and numerical model prediction in an iterative Ensemble Kalman method. Based on the inversion results, the velocity and turbulence of the flow field can be obtained. A major novelty of the present contribution is the non-parametric, full field inversion approach adopted, which is in contrast to the inference of coefficient in the ad hoc models often practiced in previous works. The merits of the proposed approach are demonstrated on the flow past a porous disk by using both synthetic data and real experimental measurements. The spatially varying drag forces of the porous disk on the flow are inferred. The proposed approach has the potential to be used in

---

\*Corresponding author. Tel: +1 540 231 0926  
*Email address:* [hengxiao@vt.edu](mailto:hengxiao@vt.edu) (Heng Xiao)

the monitoring of complex system in the above mentioned applications.

*Keywords:* inverse modeling, Ensemble Kalman filtering, actuation disk model, RANS modeling

---

## 1. Introduction

In the past several decades, the growth of computational resources along with the theoretical and algorithmic development in computational fluid dynamics (CFD) has led to a large number of commercial and open-source codes in the fields [1]. These powerful software tools have enabled scientists and engineers to numerically simulate the heat and fluid flows in complex systems at unprecedented fidelities. These numerical simulations have played critical roles in scientific enquiry, engineering design and decision making, and operational forecasting involving complex systems. For example, in commercial aircraft design, CFD simulations have largely replaced wind tunnel testing, reducing the required number of wind tunnel tests from 77 in the 1980s to less than ten in present day. Consequently, the use of CFD tools has led to drastic reduction of the development cycle duration and costs [2, 3].

The ever-increasing availability of computational resources has also expanded the application of CFD from the traditional fields of aerodynamics and hydrodynamics to a number of new areas, where the design, optimization, and other decision processes has traditionally been supported by using empirical models. Examples include simulations of the mass, heat and fluid flows in nuclear reactor vessels, the flow in wind turbine farms, the flow and convective heat transfer in data centers, and the study of sediment and turbulence in the flow through coastal vegetation plants, just to name a few. In the nuclear energy industry, CFD has been increasingly used for safety assessment of the reactor vessels in nuclear power plants [4–7]; in coastal engineering, numerical models have enabled forecasting of flood inundations, which provided valuable support for decision-making in emergence management [8]; CFD has also been used to aid heat management of data centers by modeling the heat generated by computer racks and the convective heat transfer in the rooms [9, 10].

It is well known that successful predictions of the simulations rely on faithful representations of the system geometry, initial and boundary conditions, materials properties, and

the important physics in the numerical model. However, many systems intrinsically exhibit multi-scale features that prevents first-principle based representation in numerical simulations or makes such representations very expensive. For example, a first-principle based simulation of the flow field in a wind turbine farm would require detailed representation of the rotating blades of the turbines, whose geometric features have a much smaller length scale ( $\sim 0.1$  m) than that of the wind farm (several kilometers). Similarly, a full fidelity simulation of the currents and waves in a coastal region covered with vegetation plants requires resolution of the plant geometry, which not only have complex geometries and small-scale features (e.g., stems and leafs) but are also flexible. That is, the plants deform in response to hydrodynamic forces and the effects on the flow may change accordingly. In nuclear reactor vessels, the coolant passes through thin channels in the rod bundle (fuel assembly), and the sizes of the channels are many orders of magnitude smaller than that of the reactor vessel. Because of the prohibitive computational costs of the first-principle based simulations, numerical modelings of such problems have inevitably relied on ad hoc parameterizations, which are often developed based on physics-based reasoning but with drastic simplifications. In the examples above, the wind turbines are often represented as actuation disks [11, 12], the vegetation plants are modeled as macro-roughness [13, 14], and the rod bundles in reactor vessels are often modeled as porous media with resistance. All these ad hoc models are essentially momentum sink with their resistances to the flow correlated to the local flow velocity and the physical properties of the structure (turbines or plants). The same concept can be extended to the heat and fluid flows in data centers, where the computer racks can be described as volumetric heat sources without explicitly representing their detailed geometries. While these parameterization techniques have led to significant reduction of computational costs compared to first-principle based modeling, they also introduce large model uncertainties in the numerical predictions due to their ad hoc nature.

Fortunately, the increasing availability of observation data and recent development of data assimilation algorithms [15–17] has opened new possibilities for computational mechanics simulations with parameterized models. The wide spread deployment of measurement

instrument made it possible to integrate data with numerical models in a data-driven modeling approach. For example, this data-driven approach has been explored in the modeling of wind turbine farms [18] and in quantifying uncertainty in turbulence models [19, 20]. By assimilating the available observation data, the uncertain model parameters can be inferred based on the data assimilation techniques. Although the inverse modeling has been recently used in the CFD literature to infer the coefficients in turbulence models [21, 22], an important limitation of the parametric approach is that it is still constrained by the basic assumptions of the ad hoc model and thus does not fully explore the space of model uncertainties. That is, it is possible that truth cannot be described by the chosen model regardless of how the coefficients are varied. For example, when modeling wind turbines with CFD solvers based on actuation disk model, the drag of the turbine on the flow is often made proportional to the square of the velocity in the immediate upstream of the turbine [12]. The parametric approach can only calibrate the proportionality constant but does not alter the form of the ad hoc model. To overcome this limitation, in this work we propose a non-parametric, full-field approach and use inverse modeling to infer the optimal spatial force distribution to represent the effects of complex structures based on observation data. The non-parametric approach is able to explore a much larger uncertainty space (i.e., the spatial distribution of the forces in the example of wind turbines and vegetation) than in the parametric approach. The proposed inverse modeling method is most valuable in two scenarios where observation data are available and utilized, i.e., (1) forecasting of complex systems and (2) calibrating numerical models and guiding the model development. CFD simulations are often used along with monitoring data to provide *forecasting* of complex systems. This technique, referred to as data assimilation, has long been used in operational weather forecasting [23], but its potential has also been increasingly realized in the CFD community [21, 22] and beyond. For example, the US Air Force has developed a plan to create a Digital Twin for every aircraft platform, which aims to predict the damage initiation and accumulation throughout its service life and thus provide support for decision-making in fleet management [24]. Observation data can be used to infer and calibrate the parameterization of the complex structures (e.g.,

wind turbines or vegetation), which can lead to *improvement* thereof and provide *guidance* for the model development.

In this work we use the flow past a porous disk as shown in Fig. 1 to illustrate the potential of the proposed data-driven and inverse modeling approach based on simulations with reduced order representation of the porous disk. Specifically, we performed experimental measurements and performed CFD simulations where the disks are represented with spatially varying drag force field, and then the experimental data are used to infer the optimal representation of the porous disk in the CFD simulations. The novelty lies in the non-parametric, full-field representation of the porous disks, which has implication for using computational mechanics simulations in a wide range of real-world engineering applications from nuclear power plants and wind farm to vegetation plants modeling and data centers.

The rest of the paper is organized as follows. The formulation and experimental data of the example problem, the flow past a porous disk, is presented in Section 2, and the data-driven inverse modeling approach is introduced in Section 3. Numerical results of the example problem are presented in Section 4 to assess the merits and limitation of the proposed method. The significance and limitations of the proposed inverse modeling are discussed in Section 5. Finally, Section 6 concludes the paper.

## **2. Problem Background, Formulation and Experimental Data**

In the example problem, we aim to predict the flow in the wake of a porous disk, which is often used to represent turbines (as well as propulsion devices) in lab experiments [25]. Studies on the wake of an energy-harvesting structure and its interactions with the downstream devices and the atmospheric or seabed boundary layers are of critical importance. It is because a better understanding of the corresponding flow field assists the optimization of wind turbine layout and helps to assess the environmental footprint of energy harvesting projects [11, 26–31]. A number of investigators have performed large eddy simulations to advance the understanding of the wake structure [12, 32–36]. However, as mentioned above, first-principle based simulations with full resolution of the turbine blade geometry are computationally expensive, and one often has to resort to lower fidelity models based on reduced

order representation of the turbines, particularly in operational forecasting, where a positive lead-time is required. For example, computational cost can be greatly reduced by using Reynolds-Averaged Navier–Stokes (RANS) equations to model the fluid flow and actuation disk model to represent the hydrodynamic effects of the turbines. With the actuation disk model, explicit meshing of the turbine geometry is avoided. The momentum equation of the flow field reads as follows:

$$\frac{\partial U_i}{\partial t} + \frac{\partial U_i U_j}{\partial x_j} = -\frac{1}{\rho} \frac{\partial p}{\partial x_i} + \nu \frac{\partial^2 U_i}{\partial x_j \partial x_j} - \frac{\partial \tau_{ij}}{\partial x_j} + f_i, \quad (1)$$

where  $t$  and  $x_i$  are time and space coordinates, respectively;  $\rho$  and  $\nu$  are the density and viscosity of water, respectively;  $U_i$  and  $p$  represent Reynolds-averaged velocity and pressure, respectively. The body force term  $f_i$  is a momentum sink used to account for the hydrodynamic effects of the turbines, which is often computed from actuation disk models [26] and is active only in the regions of the computational domain that are occupied by the turbines. Finally,  $\tau_{ij}$  is the Reynolds stresses computed by using an eddy viscosity model:

$$\tau_{ij} = -\frac{2}{3}k\delta_{ij} + \nu_t \left( \frac{\partial U_i}{\partial x_j} + \frac{\partial U_j}{\partial x_i} \right), \quad (2)$$

where  $\delta_{ij}$  is the Kronecker delta,  $k$  is the turbulent kinetic energy (TKE), and  $\nu_t$  is the turbulent eddy viscosity modeled by the standard two-equation  $k$ – $\varepsilon$  model [37]:

$$\frac{\partial k}{\partial t} + U_j \frac{\partial k}{\partial x_j} = P_k - \varepsilon + \frac{\partial}{\partial x_j} \left[ (\nu + \nu_t/\sigma_k) \frac{\partial k}{\partial x_j} \right] \quad (3)$$

$$\frac{\partial \varepsilon}{\partial t} + U_j \frac{\partial \varepsilon}{\partial x_j} = C_1 \frac{\varepsilon P_k}{k} - C_2 \frac{\varepsilon^2}{k} + \frac{\partial}{\partial x_j} \left[ (\nu + \nu_t/\sigma_\varepsilon) \frac{\partial \varepsilon}{\partial x_j} \right] \quad (4)$$

$$\text{with } P_k = \tau_{ij} \frac{\partial U_i}{\partial x_j} \quad (5)$$

where  $\varepsilon$  is dissipation rate,

$$\nu_t = C_\mu k^2/\varepsilon,$$

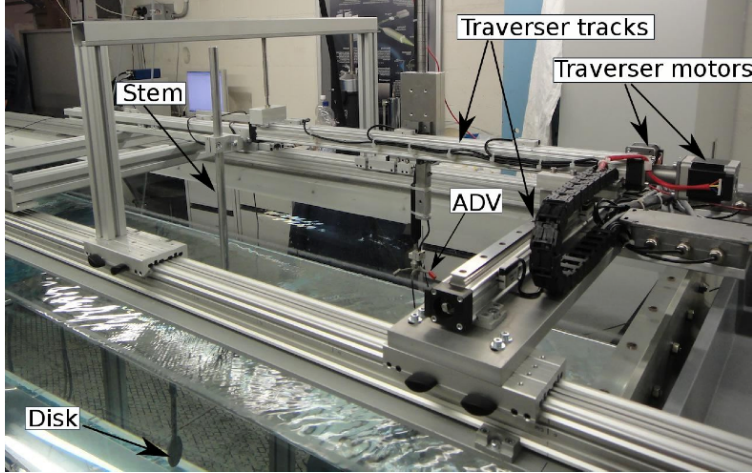
and the coefficients are:

$$C_1 = 1.44, C_2 = 1.92, C_\mu = 0.09, \sigma_k = 1.0, \sigma_\varepsilon = 1.3.$$

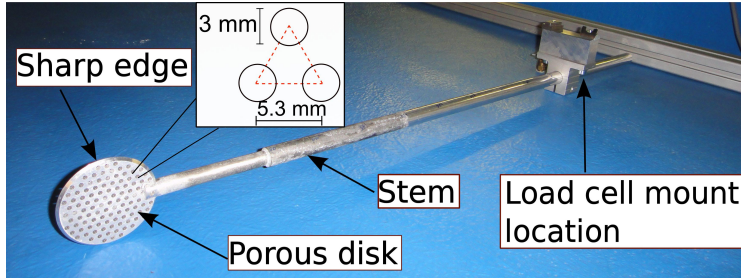
Note that the term  $P_k$  in Eq. (3) denotes the production of TKE by extracting the kinetic energy from the mean flow, which relies on the presence of the mean velocity gradient. Similarly, the term  $C_1 \frac{\varepsilon P_k}{k}$  in Eq. (4) is the production term for the dissipation rate  $\varepsilon$ .

In this work, the same set of equations and actuation disk models outlined above are used to describe the flow and the porous disk. Unlike computing the drag force  $f_i$  with an assumed force distribution in the traditional CFD modeling approaches, a number of measurements of the flow field (e.g., velocity) are incorporated in the proposed data-driven approach to infer an optimal force distribution in the region occupied by the disk. Therefore, we have conducted a laboratory experiment to measure the flow velocity and TKE in the wake of the disk. The experiment was conducted in a recirculating channel in the Institute of Fluid Dynamics at ETH Zurich (see ref. [38] for details). The dimension of test section of this channel is 2.3 m (length)  $\times$  0.45 m (width)  $\times$  0.4 m (water depth). A single porous disk is mounted on a stem inside the water channel (Fig. 1a). The disk is manufactured with a diameter of  $D = 92$  mm and thickness of  $h = 4$  mm. The holes on the disk have a diameter of 3 mm and are separated by a distance of 5.3 mm (Fig. 1b). The disk is arranged coaxially in the flow direction with its center positioned at  $2.25D$  (227 mm) above the bottom of the channel, and thus the interference of the disk with the bottom boundary layer of the channel is negligible, at least in the near-wake region studied in this work. Therefore, the mean flow can be considered axisymmetric. An acoustic Doppler velocimeter (ADV) installed on a traversing system is used to measure velocities in the wake of the disk. The detailed experimental setup is shown in Fig. 1a.

The measurements used as observations for the inverse modeling are conducted at the disk-center height in a single horizontal plane, which are on a grid of  $38 \times 18$  points with intervals of 2 cm  $\times$  2 cm, or  $0.22D \times 0.22D$ , in streamwise and spanwise directions. The measurement locations are illustrated in Fig. 2, with  $18 \times 19$  sets of velocities and TKEs measured in the downstream domain. Considering the symmetry of the disk, only half of that domain needs to be simulated. The spatial averaged measurements, located in the region surrounded with the red dashed line, are used as observation data for the inversion.



(a) Overview of the water channel



(b) The porous disk

Figure 1: (a): Overview of the water channel with the porous disk, the stem, the ADV, and the traverser system annotated with labels. The nominal water depth is 40 cm. (b) A porous disk used in this study as a simple representation of a turbine [38].

The total force  $f_t$  acted on the disk is also measured by using a six-axis load cell mounted on the stem (see Fig. 1b). The measured total force is used as the input in the proposed data-driven approach, and the objective is to infer how to distribute the force  $f_t$  over the disk.

### 3. Data-Driven Inverse Modeling Approach

In this work we proposed a data-driven, inverse modeling approach for modeling the flow with complex structures. This approach consists of two parts: reduced order representation



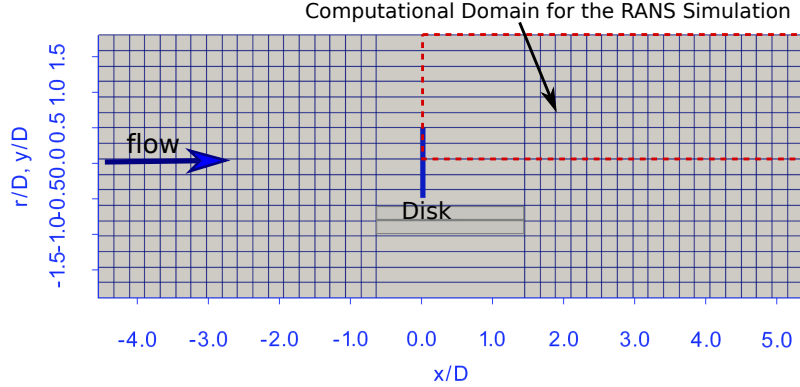


Figure 2: Locations of the velocity measurements upstream and downstream from Disk, which is indicated by a thin strip. The shown streamwise and radial coordinates are normalized by disk diameter  $D$  and the origin is located at the disk center.

of the complex structures (i.e., porous disk in the example problem), and the ensemble Kalman method based inverse modeling [17]. Specifically, the momentum sink due to the disk is represented by a non-parametric, full-field approach. Orthogonal basis functions are utilized to reduce order of the full-field force representation. The corresponding coefficients of these basis functions are inferred by incorporating the measurements of the flow quantities (e.g., velocity and turbulence kinetic energy) based on an ensemble based Kalman method. The details of the two aspects are presented below.

### 3.1. Reduced Order Representation of Momentum Sink Due to Disk

Here we only consider the drag force acting by the disk on the flow in the streamwise direction, and the force is indicated as  $f$  hereafter without ambiguity. In actuation disk theory, the drag forces are often assumed to be uniform over the disk or proportional to the amount of velocity drop across the disk. Another approach is to compute the force distribution with potential flow theory by assuming that the porosity of the disk is zero [39].

In the present approach, we allow the body force  $f(x)$  to have any physically reasonable spatial field constrained only by the axial symmetry with respect to the center of the disk.

Furthermore, we represent the field with a number of orthogonal basis functions  $\phi_\alpha$ , i.e.,

$$f(x) = f_t \Phi(x) \quad (6)$$

with  $\Phi(x) = \sum_{\alpha=1}^M w_\alpha \phi_\alpha(x)$

where  $f_t = \int_{\Omega} f(x) dx$  is the magnitude of drag force in the computational domain  $\Omega$ ,  $\Phi(x)$  is the distribution function in the domain with a normalization condition  $\int_{\Omega} \Phi(x) d\Omega = 1$ , and  $M$  is the truncated number of basis functions used to represent the force distribution. Since it is more convenient to describe the geometry of circular disk in polar coordinate  $x = (r, \theta)$ , the orthogonality of the basis functions  $\phi_\alpha(x)$  should be ensured in polar coordinate as,

$$\int_0^{2\pi} \int_0^{0.5D} \phi_\alpha \phi_\beta r dr d\theta = \delta_{\alpha\beta}, \quad \text{with } \alpha, \beta = 1, 2, \dots, M \quad (7)$$

in which  $D$  is the diameter of the disk and  $\delta_{\alpha\beta}$  denotes Kronecker delta. Commonly used basis functions (e.g., Chebyshev polynomials, Fourier series) have orthogonality only in Cartesian coordinates and not in polar coordinate. Therefore, we choose a set of orthogonal basis functions  $\phi_\alpha(r, \theta)$  in polar coordinate introduced in ref. [40], which are defined as

$$\phi_\alpha(r, \theta) = W_{m,\alpha}(r) e^{im\theta}, \quad (8)$$

where  $i$  is an imaginary unit and

$$W_{m,\alpha}(r) = r^{|m|} P_c^{(0,|m|)}(s), \quad (9)$$

and  $P_c^{(0,|m|)}(s)$  is a Jacobi polynomial with argument  $s = 2r^2 - 1$  and degree  $c = -0.5|m|$ , which are orthogonal with respect to the weight  $(1-s)^0(1+s)^{|m|}$ ; the integer  $m$  can be chosen from  $-\infty$  to  $\infty$ , which is set as  $m = 0$  in this work. The first three basis functions are  $\phi_1 = 2r^2 - 1$ ,  $\phi_2 = 6r^4 - 6r^2 + 1$ , and  $\phi_3 = 20r^6 - 30r^4 + 12r^2 - 1$ .

### 3.2. Inverse Modeling Based on Ensemble Kalman Method

With the set of orthogonal basis functions introduced above, the momentum sink due to the porous disk can be represented by  $M$  coefficients  $\boldsymbol{\omega} = [\omega_1, \dots, \omega_M]^T$  corresponding

to these basis functions. When some sparse measurements of the flow field (e.g., velocity, turbulence kinetic energy) are available, these unknown coefficients can be inferred based on the Bayesian inference approach. In this work an iterative, ensemble-based Bayesian inference method [17] is employed to perform the inversion. This technique is closely related to the ensemble-based filtering methods (e.g., ensemble Kalman filter), in which the statistical mean and covariance are estimated based on the samples [41]. An overview of the ensemble Kalman method based inverse modeling procedure is presented in Fig. 3. To infer the distribution of the force due to porous disk, the corresponding unknown coefficients  $\boldsymbol{\omega}$  are augmented to the physical state (i.e., velocity field  $\boldsymbol{u}$  and turbulence kinetic energy field  $\boldsymbol{k}$ ). The augmented state vector is denoted as  $\boldsymbol{x} \equiv [\boldsymbol{u}, \boldsymbol{k}, \boldsymbol{\omega}]^T$ , and the ensemble of the state is denoted as  $\{\boldsymbol{x}_j\}_{j=1}^N$ , where  $N$  is the number of samples. Given the observation data of the flow velocity  $\boldsymbol{u}_o$  and turbulence kinetic energy  $\boldsymbol{k}_o$ , the inversion proceeds as follows:

1. **Sampling of prior distribution.** First, one should provide an initial guess of how the force is distributed, which can be based on the physical knowledge or the low-fidelity models, e.g., actuation disk model. This initial guess is then perturbed based on one’s confidence on it. These perturbed force distributions are known as the prior ensemble. That is, given the prior for force distribution coefficients  $\boldsymbol{\omega}$ ,  $N$  samples of  $\boldsymbol{\omega}$  are drawn. Each sample represents a possible force distribution.
2. **Propagation.** In this step the flow field corresponding to each sample of the force distributions is simulated by solving the forward model (i.e., RANS equations). The physical states (i.e., velocity and turbulence kinetic energy) are predicted, and the propagated ensemble  $\{\hat{\boldsymbol{x}}_j\}_{j=1}^M$  is obtained. The mean  $\bar{\boldsymbol{x}}$  and covariance  $P$  of the propagated ensemble are estimated. Note that enough forward time steps are required to ensure that the steady state is achieved in each propagation step.
3. **Correction.** The propagated velocity and turbulence kinetic energy are compared with the observation data. Note that the dimension of observed state vector  $\boldsymbol{y}_o$  is much smaller than that of the full state  $\boldsymbol{x}$ , since the flow fields can only be measured

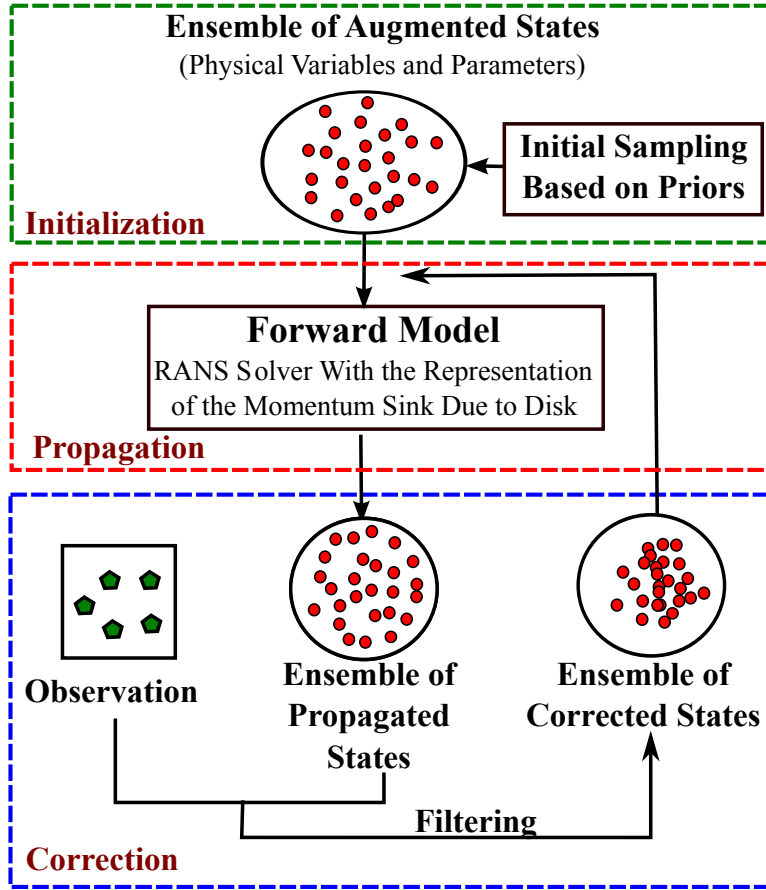


Figure 3: Schematic of the inverse modeling approach based on the state augmentation. The system state is augmented to include both the physical state (velocity and turbulence kinetic energy) and the parameters to be inferred (coefficient vector  $\omega$  for disk representation). An ensemble representing the augmented state is propagated via the forward model. The propagated ensemble is then updated in the correction process based on the observation data. The updated state (physical quantities and model parameters) is set as new initial condition, and this iteration continues until the statistical convergence is reached.

sparingly in most cases due to the intrusive nature of measurement techniques (e.g., Acoustic Doppler velocimetry). To perform the correction, the model predictions and the measurements are linearly combined. In the combination the weight of each component is determined by the Kalman gain matrix  $K$ , which is computed with the ensemble covariance  $P$  and observation error covariance  $R$ . After correction, the analyzed state contains the updated parameters of force distribution.

The propagation and correction steps (step 2 and 3) are repeated until the ensemble is statistically converged. The convergence is achieved when the variance of ensemble scattering is much smaller than the variance of the observation noise. The algorithm of the inversion scheme is summarized in Appendix A, and further detail can be found in Ref. [17].

## 4. Numerical Results

### 4.1. Verification with Synthetic Data

To establish confidence of the proposed inverse modeling approach, we conduct a synthetic case to assess its performance. In this case the observations are generated by the forward model with given “truth” of the inferred quantities, i.e., the force distribution. This specified force distribution is called as the synthetic truth, which is unknown in the inversion process. We sparsely select the velocities and turbulence kinetic energy (TKE) simulated with the synthetic truth as the synthetic observations by adding some white noise. The reason of using synthetic data (i.e., specified spatial force distribution) to verify the proposed method is that the true distribution is not available in the experiment. Only the total force acted on the disk has been measured. On the other hand, even if the truth of force distribution is known, it is still difficult to directly assess the performance of the inversion due to inadequacy of the forward model (e.g., the inadequacy in turbulence model), which poses difficulties to differentiate the errors caused by the inversion procedure and those due to the forward model.

In this work, we specify the synthetic true force distribution to be the potential flow solution by assuming that porosity of the disk is zero [39]. Consequently, the streamwise

drag force per unit area can be expressed as,

$$f(r) = f_t \lambda (1 + \tilde{\omega} r^2), \quad \text{with } 0 \leq r \leq 0.5D, \quad (10)$$

where  $\tilde{\omega} = -4.0$ , and  $\lambda$  is a normalization factor. The synthetic observation data are generated by running the forward model (i.e., RANS solver with the momentum sink) with this specified force distribution. Specifically, we choose 100 observation locations that are uniformly distributed at each of the eight spanwise lines (i.e.,  $x/D = 0.01, 0.1, 0.5, 1.0, 1.5, 2.0, 2.5$ , and  $3.0$ ). The simulated velocities and TKE on these locations are observed, and zero mean Gaussian noises ( $\epsilon_o \sim \mathcal{N}(0, \sigma_o^2)$ ) are added as the observation error, where the standard deviation  $\sigma_o$  is 1% of the truth.

The aim here is to infer the parameter  $\tilde{\omega}$  by using the proposed inversion scheme based on the synthetic observation data. By comparing the inferred result with the synthetic truth  $\tilde{\omega} = -4.0$ , the performance of inversion scheme can be evaluated. In this verification case we consider two scenarios of increasing difficulty levels. For the first scenario, the initial guesses of  $\tilde{\omega}$  are uniformly drawn from the interval of  $[-8, 0]$ , whose mean equals to the synthetic truth, i.e.,  $\mathbb{E}(\tilde{\omega}) = -4.0$ , where  $\mathbb{E}(\cdot)$  denotes expectation. That is, the prior estimation of the force distribution is unbiased. In the second scenario, a larger sampling interval of  $[-14, 0]$  with a biased mean  $\mathbb{E}(\tilde{\omega}) = -7.0$  is applied. Uniformly distributed prior is representative of lack of knowledge on the force distribution to be inferred in realistic problems. For CFD problems, the ensemble size dominates the computational costs of the inversion procedure. This is because for each sample of the force distribution, a model evaluation of RANS equation is needed to obtain the corresponding flow field, which is used to compare with the observation data in the correction step. We have studied the effects of ensemble size  $N$  on the inversion results for this problem and found that the results are not sensitive to the ensemble size when  $N$  is larger than eight. Therefore, a relatively small ensemble size of ten is adopted in this study to reduce the computational cost.

The convergence histories of parameter  $\tilde{\omega}$  in the two scenarios, starting from the unbiased prior and biased prior, are shown in Figs. 4a and 4b, respectively. The synthetic truth  $\tilde{\omega} = -4$  is also plotted for comparison. The samples of  $\tilde{\omega}$  initially scattered across the range from -8

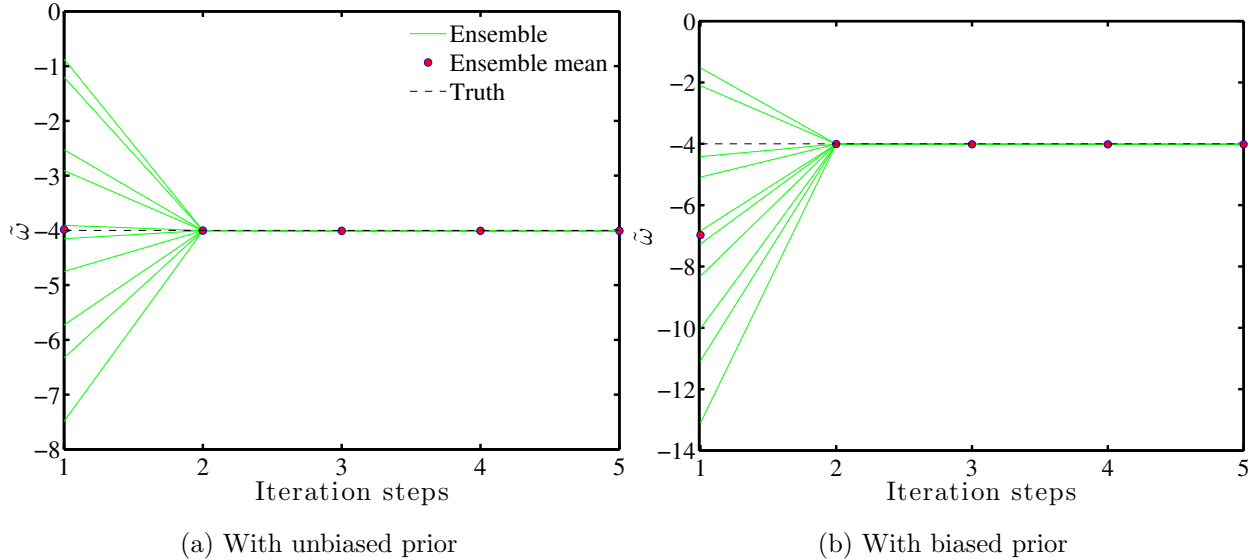


Figure 4: Convergence history of the inferred parameter  $\tilde{\omega}$  of the drag force distribution in the verification case. Synthetic truth of  $\tilde{\omega}$  is  $-4$ , to which the inverse modeling scheme is blind. The prior of  $\tilde{\omega}$  is unbiased ( $\mathbb{E}(\tilde{\omega}) = -4$ ) in panel (a), while it is biased ( $\mathbb{E}(\tilde{\omega}) = -7$ ) in panel (b), where  $\mathbb{E}(\cdot)$  denotes expectation. Note that all the samples converge and overlap with each other after the first iteration.

to 0 converge to the synthetic truth quickly (Fig. 4). Each sample of  $\tilde{\omega}$  is corrected based on the comparison of simulated and observed velocities and TKE. For the case with unbiased prior, the performance of the proposed method is excellent. However, in practice the truth is not known a priori, and thus the prior distribution is often biased. The second case is representative of the latter, more realistic scenario. For the initial samples with a biased mean and larger interval, the convergence to the truth is also achieved rapidly. All the samples and their mean are corrected to  $\tilde{\omega} = -4$ . It is worth noting that the convergences are achieved within only one iteration for both scenarios, which is because the dimension of parameter space is relatively low, and the observation data are sufficient. The importance of the prior diminishes increasing observation data. The agreement between the inferred result and the synthetic truth demonstrates the merits of the proposed inverse modeling scheme.

#### 4.2. Case with Experimental Data

A realistic inverse modeling case with the real experimental data (introduced in Sec. 2) is explored. As mentioned above, the body force  $f$  caused by the porous disk is represented by a number of basis functions with corresponding coefficients (see Eq. 6), which are to be inferred to obtain an improved flow field prediction. In this study  $M = 3$  basis functions are used to represent the force distribution. We specified a uniform distribution within  $[-10, 10]$  for the prior of each coefficient to be inferred. The magnitude of drag force is  $4.5 \times 10^{-3}$  N, which is measured from the experiment. The aim here is to infer how this drag force is distributed over the disk. We use the same sample size of  $N = 10$  as that used in the synthetic case.

The convergence histories of coefficients  $\omega_1$ ,  $\omega_2$ , and  $\omega_3$  are shown in Figs. 5a, 5b, and 5c, respectively. Similar to the synthetic case, the samples converge quickly for all the coefficients. However, a notable difference is that sample means still change with the iterations. After about 50 iterations, all the coefficients converge. Compared to the synthetic case, the convergences based on the real experimental data need more iterations. Because of the various approximations in the numerical modeling (e.g., turbulence modeling) and the measurement errors in the experimental data, a force distribution that makes the model predictions to exactly agree with the experimental observations may not exist. This is in stark contrast to the synthetic data, where the data are obtained by assuming a force distribution. Therefore, more iterations are needed to achieve statistical convergence of the samples.

The force distribution reconstructed with the converged coefficients (sample means after 100 iterations) is shown in Fig. 6. Two commonly assumed force distributions in literature are also plotted in the same figure for comparison. One is that the drag force is assumed to be uniformly distributed over the disk, which is frequently used in the literature [12, 42, 43]. The other is to assume that porosity of the disk is zero, and thus the force distribution is parabolic based on the potential flow theory [39]. The sideview of the disk are plotted with a dashed rectangular along the horizontal axis to facilitate interpretation. Based on the inversion results, the force is non-uniformly distributed on the disk with normalized



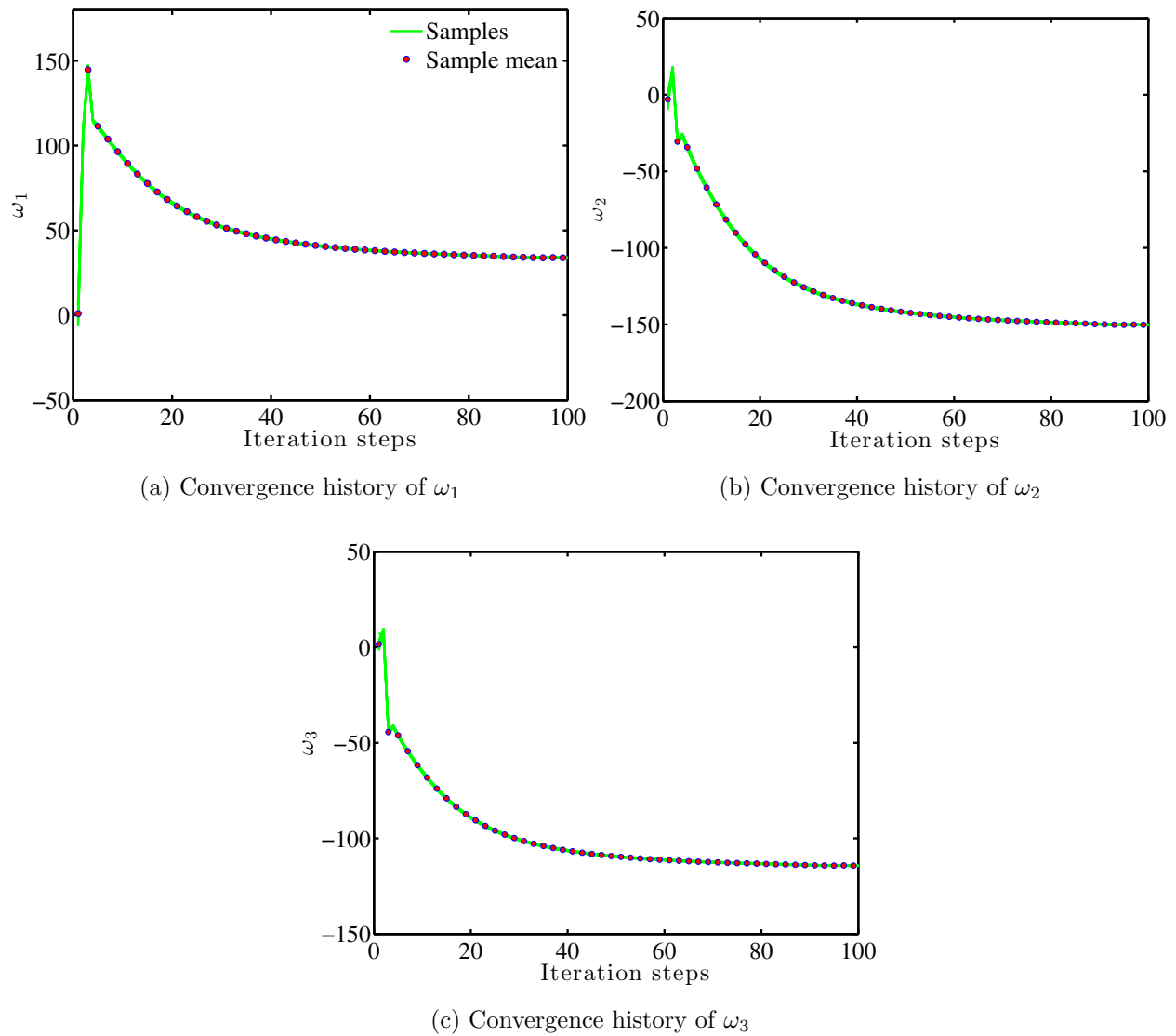


Figure 5: Convergence histories of the inferred parameters  $\omega_1$ ,  $\omega_2$  and  $\omega_3$  for the drag force distribution with experimental data. Note that the samples converge and overlap with each other after the first iteration.

magnitude from 0.7 to 1.2 (red/thick line), spatially varying around the uniformly distributed force (black/dot-dashed line). The force magnitude is smallest at the edge of the disk ( $r/D = 0.5$ ), while it peaks at near the half of its radius ( $r/D = 0.3$ ). Towards center of the disk ( $r/D = 0$ ), the force decreases and reaches a valley. Compared to the parabolic

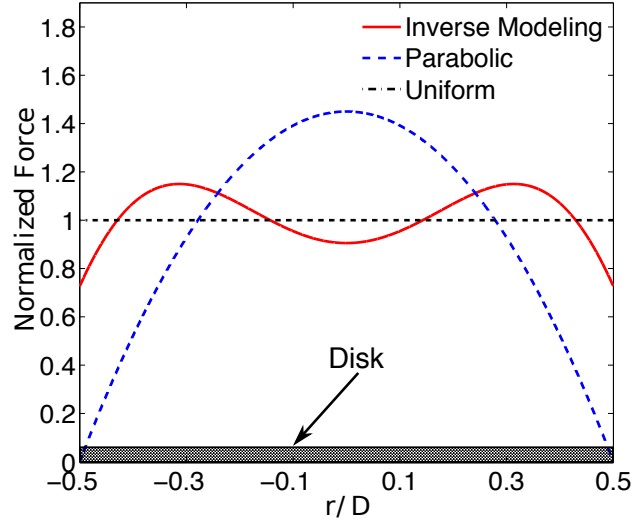


Figure 6: Estimated force distribution with the inferred parameters. The parabolic force distribution and the uniform force distribution are plotted for comparison.

force distribution (blue/dashed line), the estimated force does not have a significant decrease at the edge of disk. Another notable difference lies on the peak of the force, which is not at the disk center for the inversion result. Due to the porous structures, the force distribution of the porous disk is different from that of the solid one.

As the inference is based on the experimental data of the flow field, there is no ground truth to directly validate the inferred force distribution. Therefore, we have to evaluate it with corresponding model predictions. That is, the inferred force distribution is applied to perform a forward simulation, and the simulated flow quantities (e.g., the velocity and TKE) are compared with the experimental data to evaluate the inferred force distribution. The comparisons of the TKE profiles with the experimental data along the spanwise and streamwise directions are shown in Fig. 7. The simulated results with uniformly and parabolically distributed forces are also plotted for comparison. We only shown the results of two radial lines at  $x/D = 2.11$  and  $x/D = 2.98$  (Figs. 7a and 7b), and two streamwise lines at  $r/D = 0.154$  and  $r/D = 0.372$  (Figs. 7c and 7d). The results at other locations have similar characteristics and thus are omitted for brevity. We can see that the TKE profiles

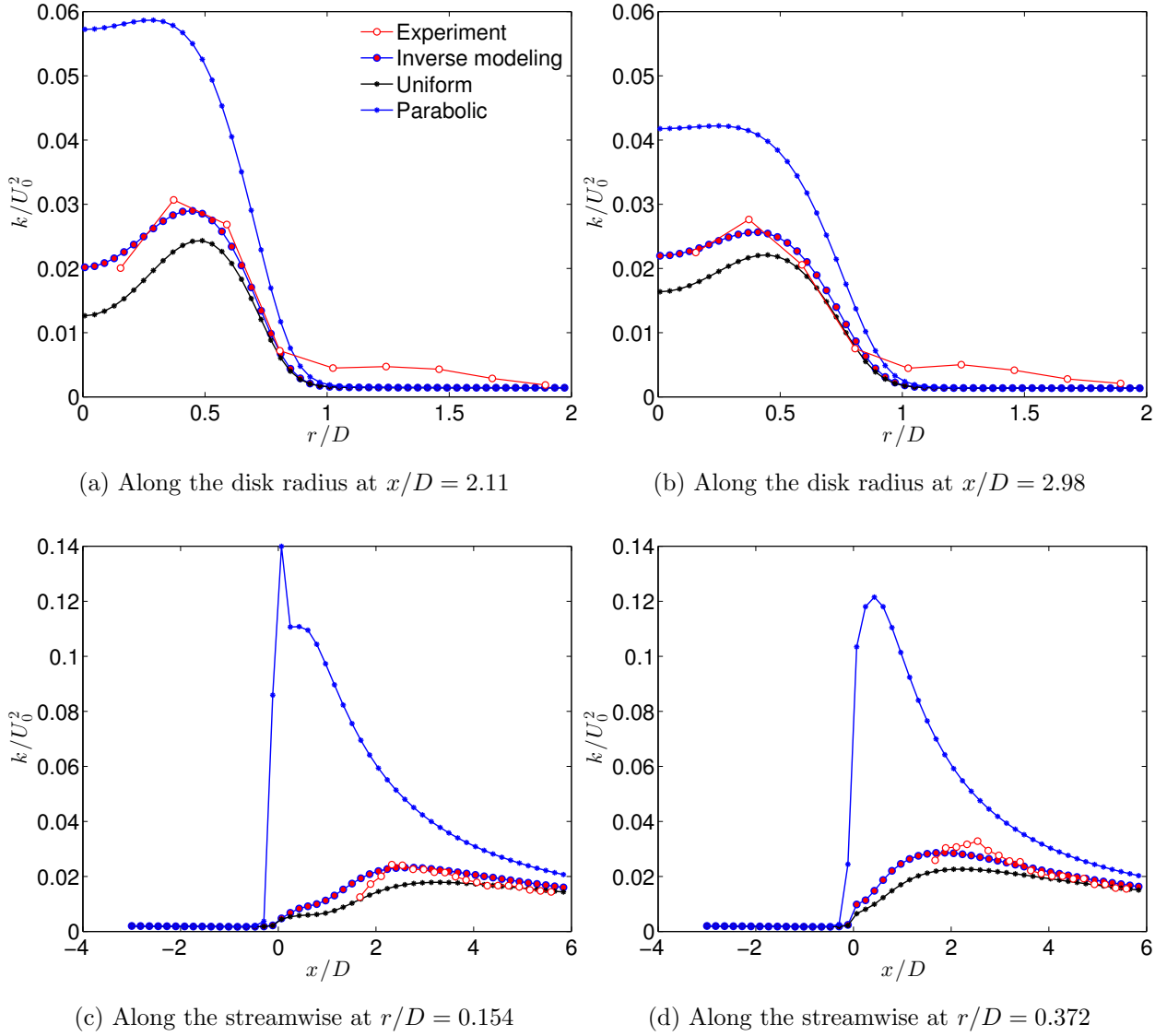
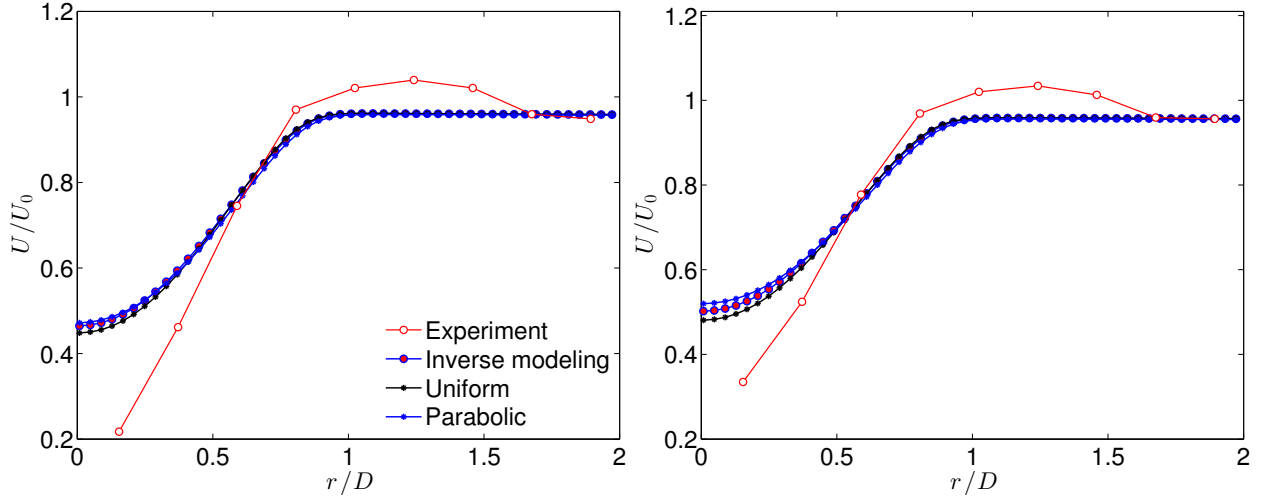


Figure 7: Comparison of turbulence kinetic energy (TKE) profiles obtained from the experiment and numerical simulations along the radial lines at (a)  $x/D = 2.11$ , (b)  $x/D = 2.98$  and along the streamwise lines at (c)  $r/D = 1.54$ , (d)  $r/D = 3.72$ .

obtained with the inferred force distribution has a better agreement with the experimental data compared to the results with the other two force distributions, especially in the wake behind the disk ( $r/D = 0 \sim 0.5$ ). In contrast, the TKE is overestimated when the parabolic

force distribution is applied, while it is underestimated as the uniform force distribution is used. In the wake at  $2.11D$  after the disk, the TKE obtained with parabolically distributed force is about twice larger than the inversion result and the experimental data (Fig. 7a), while the overestimation is reduced at  $2.98D$  after the disk (Fig. 7b). On the contrary, the TKE obtained with the uniformly distributed force is slightly smaller than the inversion result and experimental data. These trends can be also clearly seen from the TKE profiles along the streamwise directions (Fig. 7d and Fig. 7d). The results shown above indicate that the force distribution largely affects the simulated TKE, and the differences of TKE simulated with different force distributions are reduced in the far wake far region. These differences can be explained based on the momentum equation (Eq. 1). For the parabolic force distribution, the gradient  $\frac{\partial f_i}{\partial x_j}$  of the body force is overestimated because the porous structure is ignored. Overestimated force gradient amplifies the velocity gradient, which in turn leads to an increased production term in the TKE equation (Eq. 3), i.e.,  $\tau_{ij}\partial U_i/\partial x_j$ . Therefore, the turbulence kinetic energy is overestimated. On the contrary, uniform force distribution underestimates turbulence kinetic energy, since the force gradient is assumed to be zero. In contrast, the inferred force distribution markedly improves the simulation results, though discrepancies still can be seen in near-wall region ( $r/D > 1.0$ ), which might be because of the influence of wall effect of the channel in the experiment. The comparisons results shown above demonstrate merits of the proposed data-driven inverse modeling.

For the velocity prediction, a large velocity deficit exists in the wake of the disk, and it is reduced in the far wake. However, the simulated results under-predict the velocity deficit compared to the experimental data (Fig. 8). The mean velocity simulated with the inferred force distribution does not shown noticeable improvement, and the velocity profiles obtained with differently distributed forces overlap with each other, indicating that the force distribution has less influence on the velocity field of the wake. Unlike the synthetic case, more uncertain factors existed in the realistic scenarios other than the force distribution may cause this discrepancy. For example, the measured drag force  $f_t$  has uncertainties; the chosen coefficients  $C_1$  and  $C_2$  in the  $k$ - $\varepsilon$  turbulence model may not be optimal for this



(a) Along the radial direction at  $x/D = 2.11$

(b) Along the disk radial direction at  $x/D = 2.98$

Figure 8: Comparison of the mean velocity profiles obtained with different force distributions (uniform, parabolic, and inferred) along the disk radial direction at (a)  $x/D = 2.11$  and (b)  $x/D = 2.98$ . The experimental data are also plotted for comparison. Only the force distribution is calibrated in the inversion case.

particular flow. In current proposed inverse modeling scheme, all these uncertain factors also can be considered as parameters and augmented into the state, and thus they can be corrected along with the other state variables based on observation data. We demonstrate this by the following case, where the force magnitude  $f_t$  and the  $k-\varepsilon$  model constants are also considered as uncertain parameters to be inferred as well as the force distribution. For the  $k-\varepsilon$  model constants, we find  $C_1$  is most sensitive to the flow prediction for this particular flow. Therefore, for the turbulence model parameters, only  $C_1$  is to be inferred. The priors of the force magnitude  $f_t$  and turbulence constant  $C_1$  are perturbed based on  $\bar{f}_t = 0.45$  N and  $\bar{C}_1 = 1.44$ , which are the mean value of measurement data of  $f_t$  and the standard value for  $C_1$  [37], respectively. The initial samples of  $f_t$  and  $C_1$  are uniformly drawn from  $0.45 \pm 0.015$  N and  $1.44 \pm 0.2$ , respectively. The priors of force distribution parameters and other computational setup are as the same as those of the case shown above. After 100

iterations, the ensemble converges statistically. The inferred force distribution is similar as the one shown in Fig. 6. The inferred force magnitude  $f_t$  increases to  $4.57 \times 10^{-3}$  N, while the inferred turbulence constant  $C_1$  is 1.56, which is slightly larger than the standard value.

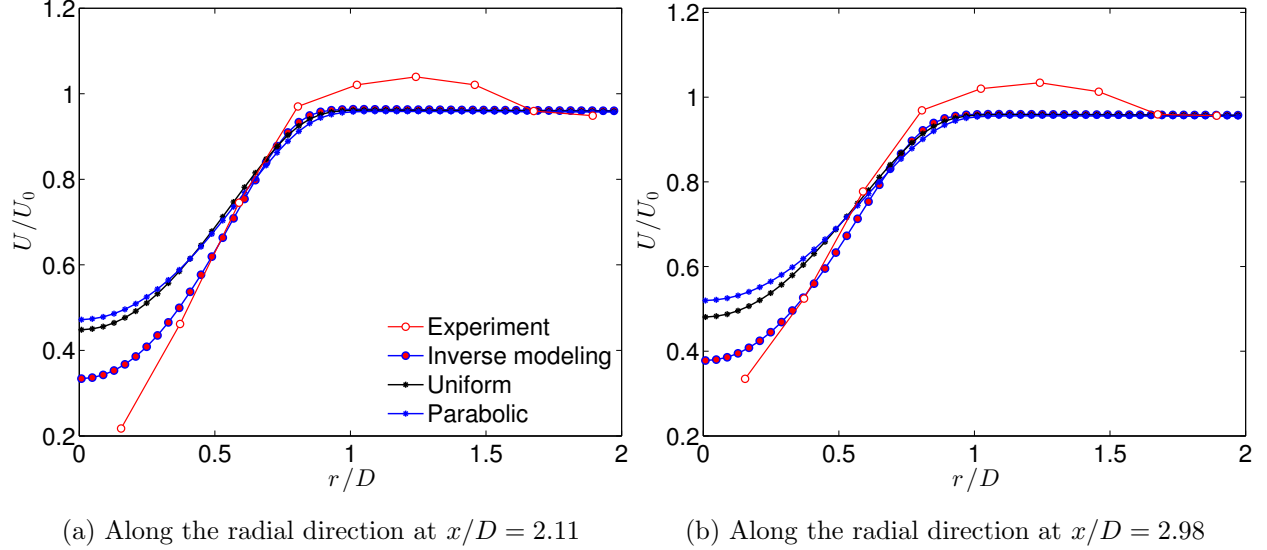


Figure 9: Comparison of the mean velocity profiles obtained with different force distributions (uniform, parabolic, and inferred) along the radial direction at (a)  $x/D = 2.11$  and (b)  $x/D = 2.98$ . The experimental data are also plotted for comparison. The force distribution, force amplitude, and turbulence model are calibrated in the inversion case.

With consideration of the uncertainties in the force distribution, force magnitude and turbulence model, both the predicted turbulence kinetic energy and velocity are significantly improved. For the turbulence kinetic energy, the predictions from inverse modeling well agrees with the experimental data, which is similar as those shown in Fig. 7 and thus is omitted for brevity. Meanwhile, the velocity predictions are also markedly improved (Fig. 9) compared to the inversion results by only considering the uncertainties in force distribution (Fig. 8). The velocity recovery in the wake, which is over-predicted in Fig. 8, has been captured more accurately here (Fig. 9). It was observed in the literature that RANS solvers based on standard turbulence models tend to overpredict the wake recovery when used in

conjunction with the actuation disk model (i.e., representing disks/turbines as momentum sinks). This deficiency was attributed to the fact that standard RANS models were not able to account for the energy transfer between the large scale turbulence associated with the coherent structures to small scale turbulence in the dissipation range, and the energy transfer mechanism is dominant in the turbine wake problem [44, 45]. Variants of the standard  $k-\varepsilon$  model have been proposed in the turbine wake modeling community to overcome this difficulty [44]. For example, in the  $k-\varepsilon-S_\varepsilon$  model proposed by El Kasami and Masson [45], a source term  $S_\varepsilon$  is added to the transport equation for the dissipation rate  $\varepsilon$  to obtain wake recovery rates in better agreement with utility scale turbine data. As mentioned earlier,  $C_1$  in the  $\varepsilon$  equation (4) is associated with the production term of the dissipation rate. Therefore, using a larger value of  $C_1$  as inferred from the wake velocity data in this work has a similar effect of boosting the production as adding a source term in the  $\varepsilon$  equation. In addition, accounting for the uncertainties in the measured force may also have contributed to the improved results as shown above, but its effects on the wake recover rate is likely to be minor. By accounting for these potential uncertainties in the model and in the experimental data and by properly representing and correcting them, the simulation results are markedly improved and better agree with the experimental data. We emphasize that the number of dimensions of the uncertainty space is large, particularly for the uncertainty in the drag force distribution on the disk. Consequently, it is not feasible to tune the coefficients manually and empirically to achieve better agreement with the experimental data. The results above demonstrates the performance of the proposed inverse modeling scheme in realistic applications with experimental data.

## 5. Discussion

In this section, we further discuss the merits and limitations of the proposed method.

### 5.1. Significance and Potential of the Data-Driven Approach

With the data-driven inverse modeling approach, the velocity and turbulent kinetic energy measurement data in the wake of a disk are used to infer the drag force incurred by the

disk, or more precisely, the drag force used to represent the hydrodynamic effects of the disk. This non-traditional modeling approach and its significance deserve further clarification. We consider two scenarios as discussed in Section 1. First, when the data-driven inverse modeling approach as presented above is utilized to provide forecasting of a farm of wind or tidal turbines, usually only sparse measure data (e.g., velocity and turbulence levels) are available. These measurements are used to infer the force distribution, which further provides the full field velocity, turbulence, and other quantities of interest. Second, when the data driven approach is used to calibrate ad hoc model or guide the developments thereof, measurement data can be available in a small number of cases, and predictions are sought for other cases without data (e.g., those with different turbines or at different operation conditions from the cases where measurements were taken). In this scenario, the spatial distribution of the drag can be extrapolated from the calibration cases to the prediction cases, where an implicit assumption is that the flow pattern between the calibration and predictions cases are indeed similar. This assumption are often valid. The merits of the present method have been demonstrated in both scenarios in the context of reducing model-form uncertainty in RANS models [19, 20], where the Reynolds stress fields and the full field velocity are inferred from sparse measurements by using the inverse modeling method present in this work. Finally, if the bimodal spatial distribution of drag forces as shown in Fig. 6 is universal among a number of turbines and flow conditions, the traditional actuation disk models can be adapted to yield such drag distributions. An important novelty of the present inverse modeling approach is that it leads to results that lend clear physical interpretations to model developers in application domains. These results are more likely to be universal than those obtained by using the parametric approach, where only the model coefficients are calibrated.

### *5.2. Limitation of the Data Driven Approach*

In the proposed inverse modeling approach, observation data are used to infer the optimal representation of complex structures in CFD simulations. The optimization is based on the how well a representation can allow the numerical simulations to reproduce the observation data. The procedure implicitly assumes that the numerical modeled system is the same



as the observed system. However, in reality this may not be true, since errors can come from many sources other than the parameterized representation of the complex structure. They include numerical discretization error, other model errors (e.g., those due to turbulence models), the discrepancies between the numerical simulation setup and the experiments (e.g., the lack of representation of water tunnel side walls). When the procedure is used in practical applications, it is possible that the inferred parameterization may be different from the most physical one. It is because the compensation for other errors that caused discrepancies between the simulated and observed responses. This error compensation may be acceptable or even desirable for operational forecasting, since it is not essential to find the most physical representation of the structure. Rather, the objective is to obtain the best prediction of the unobserved quantities and regions based the observation and the numerical model. However, when the approach is used obtain physically faithful representation of the complex structure and use it for other simulations, caution must be exercised to minimize the aforementioned discrepancies, and the remaining uncertainties should be parameterized and inferred as well.

## 6. Conclusion

Simulating the flow through complex structures is challenging due to the prohibitive computational cost of the first-principle models and the unsatisfactory fidelities of the parameterized models. In this work we proposed a data-driven, physics-based inverse modeling approach to improve the model predictions for the flow with complexed structures by incorporating sparse measurement data. The effects of complex structures are represented by a non-parametric spatial force distribution, which is inferred based on an iterative ensemble based Kalman method. The flow past a porous disk was studied as an example problem to demonstrate the merits of the proposed inverse modeling scheme. A test case with synthetic observation data is used to verify the proposed method, and the results show that the inferred force distribution agrees well with the synthetic truth. A laboratory experiment is conducted and the measurement data are used to perform a realistic inversion case. The simulation results with the inferred force distribution are compared to those with the uniformly and parabolically distributed forces and are validated by the experimental data. The

comparisons indicate that by using the proposed scheme the simulation results are markedly improved, demonstrating a satisfactory performance of the inverse modeling approach on realistic applications. The proposed data-driven inverse modeling approach is a promising tool to simulate the flows through complex structures.

## Appendix A. Iterative Ensemble Kalman Method for Inverse Modeling

The algorithm of the iterative ensemble Kalman method for inverse modeling is summarized below. See [17] for details. Given the prior of the force distributions, the follow steps are performed.

1. **(Sampling step)** Generate initial ensemble  $\{\mathbf{x}_j\}_{j=1}^N$  of size  $N$ , where the augmented system state is:

$$\mathbf{x}_j = [\mathbf{u}, \mathbf{k}, \boldsymbol{\omega}]_j$$

2. **(Prediction step)**

- (a) Propagate the state from current state  $n$  to the next iteration level  $n+1$  by solving the RANS equations (Eq. 1), indicated as  $\mathcal{F}$ ,

$$\hat{\mathbf{x}}_j^{(n+1)} = \mathcal{F}[\mathbf{x}_j^{(n)}]$$

This step involves reconstructing drag force fields for each sample and computing the velocities and turbulence kinetic energy from the RANS equations.

- (b) Estimate the mean  $\bar{\mathbf{x}}$  and covariance  $P^{(n+1)}$  of the ensemble as:

$$\bar{\mathbf{x}}^{(n+1)} = \frac{1}{N} \sum_{j=1}^N \hat{\mathbf{x}}_j^{(n+1)}$$

$$P^{(n+1)} = \frac{1}{N-1} \sum_{j=1}^N (\hat{\mathbf{x}}_j \hat{\mathbf{x}}_j^T - \bar{\mathbf{x}} \bar{\mathbf{x}}^T)^{(n+1)}$$

3. **(Correction step)**

(a) Compute the Kalman gain matrix as:

$$K^{(n+1)} = P^{(n+1)} H^T (H P^{(n+1)} H^T + R)^{-1},$$

where  $H$  is the observation matrix, which project the full states to the observed state.

(b) Update each sample in the predicted ensemble as follows:

$$\mathbf{x}_j^{(n+1)} = \hat{\mathbf{x}}_j^{(n+1)} + K(\mathbf{y}_o - H\hat{\mathbf{x}}_j^{(n+1)})$$

4. Repeat the prediction and correction steps until the ensemble is statistically converged.

## Appendix B. Notation

$c$	degree of Jacobi polynomial
$D$	diameter of the disk
$f$	thrust force
$f_t$	thrust force magnitude
$H$	observation matrix
$k$	turbulence kinetic energy
$K$	Kalman gain matrix
$\mathbf{k}$	turbulence kinetic energy state
$n$	number of mesh grids
$N$	number of basis functions used
$M$	number of samples
$p$	pressure
$P$	ensemble covariance
$r$	polar coordinate
$R$	observation error covariance
$s$	argument of Jacobi polynomial $s = 2r^2 - 1$
$t$	time coordinate

$\mathbf{u}$	velocity state
$U$	mean velocity
$V$	volume of the computational domain
$x$	spatial coordinate
$\mathbf{x}$	state vector
$\mathbf{y}_o$	observation data
Greek letters	
$\rho$	density
$\nu$	viscosity
$\tau$	Reynolds stress
$\epsilon$	dissipation rate
$\phi$	orthogonal basis function
$\omega$	coefficients for force distribution
$\boldsymbol{\omega}$	coefficients vector
$\Omega$	computational domain
$\boldsymbol{\Omega}$	normalized force distribution function
$\theta$	polar coordinate
$\delta$	Kronecker delta Subscripts/Superscripts
Decorative symbols	
$\tilde{\square}$	synthetic truth
$\bar{\square}$	mean
$\hat{\square}$	propagated state before correction
$\square'$	vector/matrix transpose
$\square_o$	observed quantity

## References

- [1] H. G. Weller, G. Tabor, H. Jasak, C. Fureby, A tensorial approach to computational continuum mechanics using object-oriented techniques, *Computers in physics* 12 (6) (1998) 620–631.
- [2] F. T. Johnson, E. N. Tinoco, N. J. Yu, Thirty years of development and application of CFD at Boeing Commercial Airplanes, seattle, *Computers & Fluids* 34 (10) (2005) 1115–1151.
- [3] F. Johnson, S. Samant, M. Bieterman, R. Melvin, D. Young, J. Bussoletti, C. Hilmes, TranAir: A full-potential, solution-adaptive, rectangular grid code for predicting subsonic, transonic, and supersonic flows about arbitrary configurations. theory document, contractor Report 4348 (1992).
- [4] U. Bieder, C. Calvin, H. Mutelle, Detailed thermal hydraulic analysis of induced break severe accidents using the massively parallel CFD code Trio-U/PRICELES, in: *Supercomputing in Nuclear Applications*, Paris, 2003.
- [5] IAEA, Use of computational fluid dynamics codes for safety analysis of nuclear reactor systems, Tech. Rep. IAEA-TECDOC-1379, International Atomic Energy Agency, Pisa, Italy, summary report of a technical meeting jointly organized by the IAEA and the Nuclear Energy Agency of the OECD (2002).
- [6] T. Höhne, U. Bieder, S. Kliem, H.-M. Prasser, A validation of TRIO-U – numerical simulations of a ROCOM buoyancy driven test case, in: *Proceedings of ICONE12, the 12th International Conference on Nuclear Engineering*, American Society of Mechanical Engineers, ASME, Arlington, VA, 2004.
- [7] D. Bertolotto, A. Manera, S. Frey, H.-M. Prasser, R. Chawla, Single-phase mixing studies by means of a directly coupled CFD/system-code tool, *Annals of Nuclear Energy* 36 (3) (2009) 310–316.

- [8] R. Luettich Jr, J. Westerink, N. W. Scheffner, ADCIRC: An advanced three-dimensional circulation model for shelves, coasts, and estuaries. report 1. theory and methodology of ADCIRC-2DDI and ADCIRC-3DL, Tech. rep., DTIC Document (1992).
- [9] H. F. Hamann, A measurement-based method for improving data center energy efficiency, in: 2008 IEEE International Conference on Sensor Networks, Ubiquitous, and Trustworthy Computing, IEEE, 2008, pp. 312–313.
- [10] H. Fernando, J. Siriwardana, S. Halgamuge, Can a data center heat-flow model be scaled down?, in: Information and Automation for Sustainability (ICIAfS), 2012 IEEE 6th International Conference on, IEEE, 2012, pp. 273–278.
- [11] I. Ammara, C. Leclerc, C. Masson, A viscous three-dimensional differential/actuator-disk method for the aerodynamic analysis of wind farms, *Journal of Solar Energy Engineering* 124 (4) (2002) 345–356.
- [12] Y.-T. Wu, F. Porté-Agel, Large-eddy simulation of wind-turbine wakes: evaluation of turbine parametrisations, *Boundary-layer meteorology* 138 (3) (2011) 345–366.
- [13] R. Masterman, C. Thorne, Predicting influence of bank vegetation on channel capacity, *Journal of Hydraulic Engineering* 118 (7) (1992) 1052–1058.
- [14] L. Doncker, P. Troch, R. Verhoeven, K. Bal, P. Meire, J. Quintelier, Determination of the manning roughness coefficient influenced by vegetation in the river Aa and Biebrza river, *Environmental Fluid Mechanics* 9 (5) (2009) 549–567.
- [15] G. Evensen, The ensemble Kalman filter: Theoretical formulation and practical implementation, *Ocean dynamics* 53 (4) (2003) 343–367.
- [16] J. Pocock, S. Dance, A. Lawless, State estimation using the particle filter with mode tracking, *Computers & Fluids* 46 (1) (2011) 392–397.
- [17] M. A. Iglesias, K. J. Law, A. M. Stuart, Ensemble Kalman methods for inverse problems, *Inverse Problems* 29 (4) (2013) 045001.

- [18] G. Iungo, F. Viola, U. Ciri, M. Rotea, S. Leonardi, Data-driven runs for simulations of large wind farms, in: *Journal of Physics: Conference Series*, Vol. 625, IOP Publishing, 2015, p. 012025.
- [19] H. Xiao, J.-L. Wu, J.-X. Wang, R. Sun, C. J. Roy, Quantifying and reducing model-form uncertainties in Reynolds-Averaged Navier-Stokes simulations: An open-box, physics-based, bayesian approach, submitted. Available at <http://arxiv.org/abs/1508.06315> (2015).
- [20] J.-L. Wu, J.-X. Wang, H. Xiao, A Bayesian calibration-prediction method for reducing model-form uncertainties with application in RANS simulations, accepted by *Flow, Turbulence and Combustion*. Available at <http://arxiv.org/abs/1510.06040> (2016).
- [21] H. Kato, S. Obayashi, Approach for uncertainty of turbulence modeling based on data assimilation technique, *Computers & Fluids* 85 (2013) 2–7.
- [22] H. Kato, A. Yoshizawa, G. Ueno, S. Obayashi, A data assimilation methodology for reconstructing turbulent flows around aircraft, *Journal of Computational Physics* 283 (2015) 559–581.
- [23] E. Kalnay, *Atmospheric modeling, data assimilation and predictability*, Cambridge university press, 2003.
- [24] B. Smarslok, A. Culler, S. Mahadevan, Error quantification and confidence assessment of aerothermal model predictions for hypersonic aircraft, in: *Proceedings of the 53rd AIAA/ASME/ASCE/AHS/ASC Structures, Structural Dynamics, and Materials*, 2012, pp. 2012–1817.
- [25] L. Myers, A. Bahaj, Experimental analysis of the flow field around horizontal axis tidal turbines by use of scale mesh disk rotor simulators, *Ocean Engineering* 37 (2) (2010) 218–227.
- [26] J. N. Sørensen, W.-Z. Shen, Numerical modeling of wind turbine wakes, *Journal of fluids engineering* 124 (2) (2002) 393–399.

- [27] L. Vermeer, J. N. Sørensen, A. Crespo, Wind turbine wake aerodynamics, *Progress in aerospace sciences* 39 (6) (2003) 467–510.
- [28] R. Gómez-Elvira, A. Crespo, E. Migoya, F. Manuel, J. Hernández, Anisotropy of turbulence in wind turbine wakes, *Journal of Wind Engineering and Industrial Aerodynamics* 93 (10) (2005) 797–814.
- [29] M. G. Gebreslassie, G. R. Tabor, M. R. Belmont, CFD simulations for investigating the wake states of a new class of tidal turbine, *Journal of Renewable Energy and Power Quality* 10 (241).
- [30] M. G. Gebreslassie, G. R. Tabor, M. R. Belmont, Numerical simulation of a new type of cross flow tidal turbine using OpenFOAM–part i: Calibration of energy extraction, *Renewable energy* 50 (2013) 994–1004.
- [31] M. G. Gebreslassie, G. R. Tabor, M. R. Belmont, Numerical simulation of a new type of cross flow tidal turbine using OpenFOAM–part ii: Investigation of turbine-to-turbine interaction, *Renewable energy* 50 (2013) 1005–1013.
- [32] M. J. Churchfield, Y. Li, P. J. Moriarty, A large-eddy simulation study of wake propagation and power production in an array of tidal-current turbines, *Philosophical Transactions of the Royal Society A: Mathematical, Physical and Engineering Sciences* 371 (1985) (2013) 20120421.
- [33] M. Calaf, C. Meneveau, J. Meyers, Large eddy simulation study of fully developed wind-turbine array boundary layers, *Physics of Fluids (1994-present)* 22 (1) (2010) 015110.
- [34] N. Troldborg, G. C. Larsen, H. A. Madsen, K. S. Hansen, J. N. Sørensen, R. Mikkelsen, Numerical simulations of wake interaction between two wind turbines at various inflow conditions, *Wind Energy* 14 (7) (2011) 859–876.
- [35] F. Porté-Agel, Y.-T. Wu, H. Lu, R. J. Conzemius, Large-eddy simulation of atmospheric boundary layer flow through wind turbines and wind farms, *Journal of Wind Engineering and Industrial Aerodynamics* 99 (4) (2011) 154–168.



- [36] X. Yang, S. Kang, F. Sotiropoulos, Computational study and modeling of turbine spacing effects in infinite aligned wind farms, *Physics of Fluids* (1994-present) 24 (11) (2012) 115107.
- [37] D. C. Wilcox, *Turbulence Modeling for CFD*, 2nd Edition, DCW Industries, 1998, Ch. 4, pp. 138–141.
- [38] H. Xiao, L. Duan, R. Sui, T. Rosgen, Experimental investigations of turbulent wake behind porous disks, *Int. J. of Heat and Mass Transfer* 15 (10) (1972) 1787–1806.
- [39] I. G. Currie, Two-dimensional potential flows, in: *Fundamental mechanics of fluids*, CRC Press, 2012, Ch. 4, pp. 73–161.
- [40] W. Verkley, A spectral model for two-dimensional incompressible fluid flow in a circular basin, *Journal of Computational Physics* 136 (1) (1997) 100–114.
- [41] G. Evensen, Sequential data assimilation with a nonlinear quasi-geostrophic model using monte carlo methods to forecast error statistics, *Journal of Geophysical Research: Oceans* (1978–2012) 99 (C5) (1994) 10143–10162.
- [42] A. Jimenez, A. Crespo, E. Migoya, J. Garcia, Advances in large-eddy simulation of a wind turbine wake, in: *Journal of Physics: Conference Series*, Vol. 75, IOP Publishing, 2007, p. 012041.
- [43] A. Jimenez, A. Crespo, E. Migoya, J. Garcia, Large-eddy simulation of spectral coherence in a wind turbine wake, *Environmental Research Letters* 3 (1) (2008) 015004.
- [44] M. Shives, C. Crawford, Adapted two-equation turbulence closures for actuator disk rans simulations of wind & tidal turbine wakes, *Renewable Energy* 92 (2016) 273–292.
- [45] A. El Kasmi, C. Masson, An extended  $k$ - $\epsilon$  model for turbulent flow through horizontal-axis wind turbines, *Journal of Wind Engineering and Industrial Aerodynamics* 96 (1) (2008) 103–122.